Monthly Notices
of the
ROYAL ASTRONOMICAL SOCIETY

MNRAS **509,** 4723–4735 (2022)
Advance Access publication 2021 November 17

https://doi.org/10.1093/mnras/stab3285

Atomic data calculations for Au I–Au III and exploration in the application of collisional-radiative theory to laboratory and neutron star merger plasmas

Michael McCann,[1]★ S. Bromley,[2] S. D. Loch[2] and C. P. Ballance[1]

[1]*CTAMOP, Queen's University Belfast, Belfast BT7 1NN, UK*
[2]*Department of Physics, Auburn University, Auburn, AL 36832, USA*

Accepted 2021 November 9. Received 2021 November 8; in original form 2021 June 18

ABSTRACT

Neutron binary star mergers have long been proposed as sufficiently neutron rich environments that could support the synthesis of rapid neutron capture elements (r-process elements) such as gold. However, the literature reveals that beyond neutral and singly ionized systems, there is an incompleteness of atomic data for the remaining ion stages of importance for mergers. In this work, we report on relativistic atomic structure calculations for Au I–Au III using the GRASP^0 codes. Comparisons to calculations using the Flexible Atomic Code suggest uncertainties on average of 9.2 per cent, 5.7 per cent, and 3.8 per cent for Au I–Au III level energies. Agreement around ∼50 per cent is achieved between our computed A-values and those in the literature, where available. Using the GRASP^0 structure of Au I, we calculated electron-impact excitation rate coefficients and use a collisional-radiative model to explore the excitation dynamics and line ratio diagnostics possible in neutron star merger environments. We find that proper accounting of metastable populations is critical for extracting useful information from ultraviolet–visible line ratio diagnostics of Au I. As a test of our data, we applied our electron-impact data to study a gold hollow cathode spectrum in the literature and diagnosed the plasma conditions as $T_e = 3.1 \pm 1.2$ eV and $n_e = 2.7^{+1.3}_{-0.9} \times 10^{13}$ cm^{-3}.

Key words: atomic data – neutron star mergers – line: identification – plasmas – scattering – techniques: spectroscopic.

1 INTRODUCTION

With the advent of detecting gravitational waves from a binary neutron star merger (NSM) by the laser interferometer gravitational-wave observatory (LIGO) collaboration and follow-up studies of the electromagnetic counterpart(s) (Coulter et al. 2017), interest in heavy r-process elements has increased dramatically. Immediately following an NSM, physical conditions are expected to produce significant abundances of r-process elements, including the lanthanides, actinides, and platinum-group elements (Kajino et al. 2019). Given their expected contributions to NSM spectra, both atomic, molecular and optical (AMO) theorists and experimentalists have received increasing demand to determine spectral emission and atomic data for these elements.

Disentangling r-process abundances from the broad spectra of NSM GW170817 is a formidable task that demands a high degree of rigour in calculations of the ejecta opacity and the atomic calculations that underpin them. A recent paper by Fontes et al. (2020) highlights that lanthanides with open f-shell configurations may contribute to NSM opacities much more than Fe-peak elements. However, whereas Fe-peak elements have been well studied over the last decades, elements beyond $Z \geq 75$ have received less attention. A single open f-shell configuration may produce over a hundred $J\pi$ resolved levels, which when combined with the strong configuration interaction mixing for near-neutral heavy systems ensures that achieving convergence for both energy levels and Einstein A-values is difficult. This point is echoed in Kramida (2019), which summarizes that current theoretical calculations are insufficient to match observed spectra. While excellent agreement at the ∼cm^{-1} level is possible with the orthogonal operators approach (cf. Uylings & Raassen 2019), its application is currently limited to a select number of cases and not yet available in a generalized form. However, it is possible to improve the accuracy of calculated atomic data by benchmarking against lab spectra and re-scaling to experimental quantities where possible. Indeed, the success of Cowan's structure codes (Cowan 1981) relies on such a parametric fitting to observed emission spectra.

Our calculations are informed by two ongoing efforts, spanning both astrophysical and laboratory plasma regimes. Experimental measurements of Au I and Au II spectra in Bromley et al. (2020) showed the complexity of excitation at moderately high temperatures (∼30 eV) and densities ($n_e \sim 10^{12}$ cm^{-3}) of the Compact Toroidal Hybrid experiment (Hartwell et al. 2017). At the lower temperatures (∼eV) and densities (∼10^9 cm^{-3}) expected in NSM ejecta ∼1 d post-merger (Gillanders et al. 2021), the long time-scales between excitation (either through photonic or electronic collisions) and collisional de-excitation suggest that metastable populations may have a significant effect on observed line intensities.

To aid both future and existing efforts in laboratory and astrophysical applications, we report herein relativistic structure calculations

★ E-mail: mmccann80@qub.ac.uk

of Au I–Au III and electron-impact data generation for Au I. For the atomic structures, we use a modified version of the GRASP^0 code (Parpia, Froese Fischer & Grant 1996) for Dirac–Coulomb Hamiltonians determined from a Multi-Configuration Dirac–Fock (MCDF) approach. Our GRASP^0 calculations were recently used by Gillanders et al. (2021) to search for evidence of Au/Pt emission in optical spectra of GW170817. For both low-temperature and high-temperature regimes, atomic data are much less useful when wavelengths are not at spectroscopic accuracy, severely limiting the identification and application of line ratios for diagnostic purposes. Atomic data are further less useful when uncertainties of the atomic data cannot be assessed. As an independent check on the GRASP^0 calculations, we report similar calculations using FAC (Flexible Atomic Code; Gu 2008) to assess the accuracy of our target level designations and their respective energies. Where possible, we have compared subsets of our calculated data (levels, E1 rates) to measurements from the gold literature, including Platt & Sawyer (1941), Ehrhardt & Davis (1971), Rosberg & Wyart (1997), Zainab & Tauheed (2019), and Bromley et al. (2020), to ensure proper level matching. Though electron-impact data presented here are restricted to Au I, these comparisons validate the GRASP^0 results for electronic structure that shall be utilized in future calculations of Au II and Au III electron-impact excitation.

The remainder of the paper is structured as follows. In Section 2, we briefly describe how we optimized the orbitals for each of first three ion stages of Au. A discussion of our FAC calculations and additional insights gleaned from their results are also provided. In Section 3, we describe the relativistic electron-impact excitation calculation for Au I, with the associated Maxwellian-averaged collision strengths discussed. In Section 4, we explore the capabilities of our electron-impact data and identify complexities at low temperatures and densities. In Section 5, we summarize our results and their implications for future studies of the first three ion stages of Au.

2 ATOMIC STRUCTURE MODELS

In the following, we describe our atomic structure calculations for Au I–Au III. We have focused our efforts on the lowest configurations that are expected to be excited in either laboratory or astrophysical plasma temperature and density regimes. Our goal is to provide a compact representation of these ion stages and determine the dominant populating mechanisms in the subsequent collisional calculations, ultimately to identify strong lines, which may form the basis of temperature, density, or metastable diagnostics.

To improve the accuracy of the calculated transition rates, we utilize the functionality in both GRASP^0 and FAC to shift level energies to experimentally determined values in the NIST ASD (Kramida et al. 2020) prior to calculating transition rates. For dipole-allowed transitions, the transition rate from level k to i is written as

$$A_{ki} = \frac{16\pi^3}{3h\epsilon_0\lambda^3 g_k} S, \tag{1}$$

where S is the line strength calculated from the wavefunctions of levels k and i, λ is the vacuum wavelength of the transition, g_k is the statistical weight of level k, ϵ_0 is the vacuum permittivity, and h is the Planck constant. While our energy level shifting leaves the wavefunctions unaffected, the transition rate is re-scaled by the tuning of the energy difference of the upper and lower levels. For weaker E2 and M2 transitions that may affect the metastable populations in a collisional environment, the transition rate is proportional to δE_{ki}^5, and is thus expected to depend strongly on accurate energies.

2.1 GRASP^0 calculations

To generate optimized orbitals for Au I–Au III, we employ the relativistic atomic structure package GRASP^0 (Parpia et al. 1996), which uses the MCDF method to generate bound orbitals within an extended average level approximation. Using the literature as a guide, we incorporated the configurations that most strongly interact via configuration interaction among the lowest levels and are most likely to impact subsequent electron-impact excitation calculations. Where possible, we note which levels correspond to those identified in literature, and have shifted them appropriately prior to calculating transition rates.

We note that the $n = 6$ orbitals of these heavy systems have a significant number of nodes in the radial wavefunctions. This equates to a great sensitivity in the A-value when calculating the overlap between two oscillating wavefunctions. Recall that the line strength is given by

$$S = |R_{ik}|^2,$$
$$R_{ik} = \langle \psi_k | P | \psi_i \rangle , \tag{2}$$

where ψ_i and ψ_k are the initial and final state wavefunctions, and R_{ik} is the transition matrix element of the multipole operator P. For orbitals with a large number of nodes, for example, the 6s orbital of Au I, we found that the line strength is particularly sensitive to how each orbital is optimized. Large changes in dipole (E1) transition rates are apparent depending on whether the 6s orbital is optimized on $5d^{10}6s$ or $5d^96s^2$. In this work, we found that optimizing the 6s orbital for the configuration $5d^96s^2$ led to dipole (E1) transition rates closer to experimentally determined transition rates.

2.1.1 Au I

For Au I, the NIST ASD (Kramida et al. 2020) has 75 energy levels and 191 lines, only 20 of which have reported transition rates. Our GRASP^0 structure for Au I incorporated a total of 14 non-relativistic configurations, 10 of which were even parity and 4 were odd parity. The configurations used by both GRASP^0 and FAC for Au I are shown in Table 1. The 10 even configurations were $5d^{10}6s$, $5d^96s^2$, $5d^96p^2$, $5d^{10}6d$, $5d^96d^2$, $5d^86d^3$, $5d^86s6p^2$, $5d^76s^26p^2$, $5d^86s^26d$, and $5d^76s^26d^2$, while the 4 odd configurations are $5d^{10}6p$, $5d^86p^3$, $5d^96s6p$, and $5d^86s^26p$. These configurations resulted in a total of 2202 $J\pi$ energy levels. This choice of configurations strikes the balance between achieving a reasonable representation of the target while maintaining the feasibility of implementing the R-matrix electron-impact calculation to follow.

A comparison of the first 26 NIST energy levels to the GRASP^0 and FAC calculations is shown in Table 2. Energies are shown with respect to the ground level $5d^{10}6s$. For Au I, the energies of the first 26 levels were shifted to their experimental values prior to calculating transition rates. The average difference between the calculated energies and experimentally determined energies in Platt & Sawyer (1941) and Ehrhardt & Davis (1971) is 8.6 per cent.

Table 3 shows a comparison of some Au I transition rates with experimental values from the NIST ASD. The average agreement for these lines with GRASP^0 is 29.16 per cent, with the GRASP^0 results showing better agreement than the FAC results with an average agreement of 46.53 per cent between FAC and NIST.

Table 1. Configurations used for the GRASP^0 and FAC calculations of Au I energy levels and transition rates.

Calculation	Configurations
GRASP^0 / FAC1	$5d^{10}6s$, $5d^{10}6p$, $5d^{10}6d$, $5d^96s^2$, $5d^96p^2$, $5d^96d^2$, $5d^86p^3$, $5d^86d^3$, $5d^96s6p$, $5d^86s6p^2$, $5d^86s^26p$, $5d^76s^26p^2$, $5d^86s^26d$, $5d^76s^26d^2$
FAC2 = FAC1 +	$5d^{10}7s$, $5d^{10}7p$, $5d^97s^2$, $5d^97p^2$, $5d^96s6d$, $5d^96s7s$, $5d^96s7p$, $5d^86s^27s$, $5d^86s^27p$, $5d^76s^26p6d$, $5d^76s^26p7s$, $5d^76s^27s7p$, $5d^76s^26p7p$, $5d^76s^26d7s$, $5d^76s^27s^2$, $5d^{10}5f$, $5d^{10}6f$, $5d^{10}7d$, $5d^{10}7f$, $5d^{10}8s$, $5d^{10}8d$, $5d^{10}8p$, $5d^{10}8f$, $5d^95f6f$, $5d^95f7s$, $5d^95f7d$, $5d^95f8s$, $5d^95f8d$, $5d^96s5f$, $5d^96s6f$, $5d^96s7d$, $5d^96s7f$, $5d^96s8s$, $5d^96s8p$, $5d^96s8d$, $5d^96s8f$, $5d^96p7p$, $5d^96p6d$, $5d^96p7s$, $5d^96p7d$, $5d^96p8s$, $5d^96p8d$, $5d^96d7s$, $5d^96d7p$, $5d^96d7d$, $5d^96d8s$, $5d^96d8p$, $5d^96d8d$, $5d^97s7p$, $5d^97s7d$, $5d^97s7f$, $5d^97p7d$, $5d^97d^2$, $5d^98s^2$, $5d^98s8p$, $5d^98p8d$, $5d^98p^2$, $5d^98d^2$, $5d^85f^3$, $5d^86s^25f$, $5d^86s6p^2$, $5d^86p^3$, $5d^86s6p6d$, $5d^86s6d^2$, $5d^86p^26d$, $5d^86p6d^2$, $5d^86d^3$, $5d^86s6p7s$, $5d^86s6p7p$, $5d^86s^27d$, $5d^86s6p7d$, $5d^86p7s^2$, $5d^86p7p^2$, $5d^86p7d^2$, $5d^86s6d7s$, $5d^86s6d7p$, $5d^86s6d7d$, $5d^86s7s^2$, $5d^86s7p^2$, $5d^86s7d^2$, $5d^86s8s^2$, $5d^86s8p^2$, $5d^86s8d^2$, $5d^86s6p8s$, $5d^86s6p8p$, $5d^86s6p8d$, $5d^86p8s^2$, $5d^86p8p^2$, $5d^86p8d^2$, $5d^86p7s7p$, $5d^86s^28s$, $5d^86s^28p$, $5d^86s^28d$, $5d^76s6p^3$, $5d^76p^4$, $5d^76s6p^26d$, $5d^76s6p6d^2$, $5d^76s6p5f^2$, $5d^76s6p6f^2$, $5d^76s6d^3$, $5d^76d^4$, $5d^76s^26p^2$, $5d^76s^26d^2$, $5d^76s^27p^2$, $5d^76s^27d^2$, $5d^76p^26d^2$, $5d^76s6p^27s$, $5d^76s6p^27p$, $5d^76s6p7s^2$, $5d^76s6p7p^2$, $5d^76s6p7d^2$, $5d^76s^28s^2$, $5d^76s^28s8p$, $5d^76s^28p^2$, $5d^76s^28s8d$, $5d^76s^28d^2$

Table 2. Energies of the first 26 energy levels of Au I from literature, compared to our GRASP^0 and FAC calculations.

Level	Conf.	Term	Parity	J	Literature (Ryd)	GRASP^0 (Ryd)	GRASP^0 (% diff)	FAC2 (Ryd)	FAC2 (% diff)
1	$5d^{10}6s$	^{2}S	Even	1/2	0.0000	0.0000	0.00	0.0000	0.00
2	$5d^96s^2$	^{2}D	Even	5/2	0.0835	0.0613	− 26.56	0.1393	66.85
3	$5d^96s^2$	^{2}D	Even	3/2	0.1953	0.1760	− 9.87	0.2584	32.28
4	$5d^{10}6p$	^{2}P	Odd	1/2	0.3404	0.3592	5.52	0.3096	− 9.07
5	$5d^{10}6p$	^{2}P	Odd	3/2	0.3752	0.3728	− 0.63	0.3383	− 9.83
6	$5d^96s6p$	^{4}P	Odd	5/2	0.3842	0.3665	− 4.61	0.4066	5.82
7	$5d^96s6p$	^{4}F	Odd	7/2	0.4150	0.4184	0.83	0.4470	7.72
8	$5d^96s6p$	^{4}F	Odd	5/2	0.4208	0.4255	1.12	0.4559	8.34
9	$5d^96s6p$	^{4}D	Odd	5/2	0.4226	0.4847	14.68	0.5170	22.34
10	$5d^96s6p$	^{4}P	Odd	3/2	0.4284	0.4257	− 0.63	0.4618	7.81
11	$5d^96s6p$	^{4}F	Odd	9/2	0.4438	0.4374	− 1.43	0.4757	7.20
12	$5d^96s6p$	^{4}D	Odd	7/2	0.4650	0.4755	2.25	0.5086	9.37
13	$5d^96s6p$	^{2}D	Odd	3/2	0.4669	0.4737	1.46	0.5113	9.51
14	$5d^96s6p$	^{4}F	Odd	3/2	0.4692	0.5216	11.17	0.5522	17.70
15	$5d^96s6p$	^{2}D	Odd	5/2	0.4707	0.6027	28.04	0.6318	34.22
16	$5d^96s6p$	^{2}F	Odd	7/2	0.4812	0.5941	23.48	0.6540	35.92
17	$5d^96s6p$	^{4}P	Odd	1/2	0.4848	0.4879	0.65	0.5273	8.78
18	$5d^96s6p$	^{4}D	Odd	1/2	0.5079	0.5670	11.64	0.6024	18.62
19	$5d^96s6p$	^{4}D	Odd	3/2	0.5113	0.5872	14.84	0.6251	22.26
20	$5d^96s6p$	^{2}F	Odd	5/2	0.5342	0.5513	3.22	0.5841	9.35
21	$5d^96s6p$	^{2}P	Odd	3/2	0.5362	0.5935	10.67	0.6132	14.36
22	$5d^96s6p$	^{2}F	Odd	5/2	0.5441	0.7680	41.14	0.7551	38.77
23	$5d^96s6p$	^{2}D	Odd	5/2	0.5582	0.6767	21.23	0.6601	18.25
24	$5d^96s6p$	^{2}D	Odd	3/2	0.5610	0.7859	40.09	0.7868	40.25
25	$5d^{10}6d$	^{2}D	Even	3/2	0.5645	0.5927	4.98	0.5019	− 11.09
26	$5d^{10}6d$	^{2}D	Even	5/2	0.5653	0.5896	4.30	0.5023	− 11.14

The differences between the energies given by the GRASP^0 and the FAC calculations relative to the measured energies in literature (Platt & Sawyer 1941; Ehrhardt & Davis 1971) are shown as a percentage. Note that for the $5d^96s6p$ levels there is significant mixing for levels above level 15.

Table 3. Representative comparison of A-values for E1 transition rates of Au I in the NIST ASD.

Transition levels	Configuration	A-value (s^{-1}) GRASP^0	FAC2	NIST
1 → 4	$5d^{10}6s\ ^2S_{1/2} \rightarrow 5d^{10}6p\ ^2P^0_{1/2}$	1.61E+08	2.46E+08	1.64E+08
1 → 5	$5d^{10}6s\ ^2S_{1/2} \rightarrow 5d^{10}6p\ ^2P^0_{3/2}$	2.26E+08	3.17E+08	1.98E+08
2 → 5	$5d^96s^2\ ^2D_{5/2} \rightarrow 5d^{10}6p\ ^2P^0_{3/2}$	2.60E+07	1.34E+07	1.90E+07
2 → 7	$5d^96s^2\ ^2D_{5/2} \rightarrow 5d^9_{5/2}6s_{1/2}6p_{1/2}\ ^4F^0_{7/2}$	1.43E+06	6.65E+06	1.03E+07
3 → 4	$5d^96s^2\ ^2D_{3/2} \rightarrow 5d^{10}6p\ ^2P^0_{1/2}$	2.33E+06	1.46E+06	3.40E+06
3 → 5	$5d^96s^2\ ^2D_{3/2} \rightarrow 5d^{10}6p\ ^2P^0_{3/2}$	4.98E+05	2.75E+05	5.20E+05

Table 4. Energies of the first 30 energy levels of Au II from Rosberg & Wyart (1997), compared to our GRASP^0 and FAC calculations.

Level	Conf.	Term	Parity	J	R & W (Ryd)	GRASP^0 (Ryd)	GRASP^0 (% diff)	FAC2 (Ryd)	FAC2 (% diff)
1	$5d^{10}$	^{1}S	Even	0	0.0000	0.0000	0.00	0.0000	0.00
2	$5d^9 6s$	^{3}D	Even	3	0.1370	0.1299	− 5.20	0.1418	3.47
3	$5d^9 6s$	^{3}D	Even	2	0.1608	0.1598	− 0.61	0.1700	5.71
4	$5d^9 6s$	^{3}D	Even	1	0.2530	0.2454	− 3.01	0.2568	1.50
5	$5d^9 6s$	^{1}D	Even	2	0.2699	0.2710	0.39	0.2800	3.73
6	$5d^8 6s^2$	^{3}F	Even	4	0.3689	0.4164	12.90	0.4166	12.92
7	$5d^8 6s^2$	^{3}P	Even	2	0.4421	0.5016	13.47	0.5517	24.79
8	$5d^8 6s^2$	^{3}F	Even	3	0.4755	0.5285	11.16	0.5258	10.58
9	$5d^8 6s^2$	^{3}F	Even	2	0.5303	0.5953	12.25	0.5077	-4.27
10	$5d^8 6s^2$	^{3}P	Even	0	0.5335	0.6027	12.96	0.6162	15.50
11	$5d^8 6s^2$	^{3}P	Even	1	0.5627	0.6388	13.53	0.6439	14.43
12	$5d^9 6p$	(5/2,1/2)	Odd	2	0.5746	0.5400	− 6.02	0.5517	− 3.99
13	$5d^9 6p$	(5/2,1/2)	Odd	3	0.5924	0.5720	− 3.44	0.5794	− 2.19
14	$5d^8 6s^2$	^{1}G	Even	4	0.5951	0.6703	12.63	0.6717	12.87
15	$5d^8 6s^2$	^{1}D	Even	2	0.6451	0.7148	10.79	0.7155	10.92
16	$5d^9 6p$	(5/2,3/2)	Odd	4	0.6606	0.6302	− 4.61	0.6376	− 3.48
17	$5d^9 6p$	(5/2,3/2)	Odd	2	0.6668	0.6425	− 3.65	0.6481	− 2.8
18	$5d^9 6p$	(5/2,3/2)	Odd	1	0.6689	0.6372	− 4.73	0.6444	− 3.65
19	$5d^9 6p$	(5/2,3/2)	Odd	3	0.6815	0.6622	− 2.84	0.6654	− 2.36
20	$5d^9 6p$	(3/2,1/2)	Odd	2	0.6986	0.6791	− 2.78	0.6851	− 1.92
21	$5d^9 6p$	(3/2,1/2)	Odd	1	0.7441	0.7490	0.65	0.7477	0.49
22	$5d^9 6p$	(3/2,3/2)	Odd	0	0.7528	0.7159	− 4.91	0.7233	− 3.91
23	$5d^9 6p$	(3/2,3/2)	Odd	3	0.7810	0.7603	− 2.65	0.7603	− 2.41
24	$5d^9 6p$	(3/2,3/2)	Odd	1	0.7810	0.7791	− 0.25	0.7683	− 1.62
25	$5d^9 6p$	(3/2,3/2)	Odd	2	0.7888	0.7720	− 2.13	0.7732	− 1.97
26	$5d^8(^3F)6s6p$	^{5}D	Odd	3	0.7912	0.8215	3.83	0.8052	1.77
27	$5d^8(^3F)6s6p$	^{5}G	Odd	4	0.8031	0.8356	4.05	0.8235	2.54
28	$5d^8(^3P)6s6p$	^{5}P	Odd	2	0.8235	0.8631	4.81	0.8538	3.67
29	$5d^8(^3F)6s6p$	^{5}G	Odd	3	0.8411	0.8757	4.12	0.8656	2.91
30	$5d^8(^1D)6s6p$	^{3}F	Odd	2	0.8523	0.8967	5.20	0.8886	4.26

The differences between the energies given by the GRASP^0 and the FAC calculations relative to the Rosberg & Wyart (1997) energies are shown as a percentage.

Table 5. Representative comparison of A-values from Rosberg & Wyart (1997) compared to the present GRASP^0 and FAC2 calculations.

Transition levels	Configuration	A-value (s^{-1}) GRASP^0	FAC2	Rosberg & Wyart
1 → 18	$5d^{10}\,^1S_0 \rightarrow 5d^9 6p\,^3P^0_1$	8.96E+07	1.07E+08	3.59E+08
1 → 21	$5d^{10}\,^1S_0 \rightarrow 5d^9 6p\,^3D^0_1$	2.12E+08	5.18E+08	3.70E+09
1 → 24	$5d^{10}\,^1S_0 \rightarrow 5d^9 6p\,^1P^0_1$	1.65E+09	1.00E+09	2.14E+09
2 → 13	$5d^9\,^3D_3 \rightarrow 5d^9 6p\,^3P^0_2$	4.08E+08	1.37E+08	2.27E+09
2 → 16	$5d^9\,^3D_3 \rightarrow 5d^9 6p\,^3F^0_4$	7.27E+08	6.13E+08	7.81E+09
2 → 17	$5d^9\,^3D_3 \rightarrow 5d^9 6p\,^1D^0_2$	1.05E+07	1.22E+07	2.31E+08

Additionally, a calculation using GRASP^0 was performed, which included pseudo-states up to $n = 8$, including 26 non-relativistic configurations and 2406 energy levels. However, this only resulted in a change of the transition rates shown in Table 3 by 4.89 per cent on average.

2.1.2 *Au II*

The most comprehensive data for Au II lines and levels come from Rosberg & Wyart (1997), who classified 121 levels and computed gf values for ∼450 transitions. For the GRASP^0 calculation of Au II, 14 configurations in total were employed: 11 even configurations $5d^{10}$, $5d^9 6s$, $5d^9 6d$, $5d^9 7s$, $5d^9 7d$, $5d^8 6s^2$, $5d^8 6p^2$, $5d^8 7s^2$, $5d^8 7p^2$, $5d^8 6s7s$, and $5p^4 5d^{10} 6s^2$, and the 3 odd configurations $5d^9 6p$, $5d^9 7p$, and $5d^8 6s6p$. This resulted in a total of 436 energy levels.

Table 4 shows the first 30 levels of Au II, which encompasses the even configurations $5d^{10}$, $5d^9 6s$, and $5d^8 6s^2$. The lowest odd levels of Au II primarily belong to $5d^9 6p$, with some of the more highly excited levels belonging to $5d^8 6s6p$. Agreement between the computed energies of the odd levels and the experimentally determined energies from Rosberg & Wyart (1997) is of the order of approximately a few per cent. In total, the average difference between the GRASP^0 and Rosberg & Wyart (1997) energies for the first 30 energy levels is 5.1 per cent.

Table 6. Energies of the first 30 energy levels of Au III from literature (Ehrhardt & Davis 1971; Zainab & Tauheed 2019), compared to our GRASP^0 and FAC calculations.

Level	Conf.	Term	Parity	J	Literature (Ryd)	GRASP^0 (Ryd)	GRASP^0 (% diff)	FAC2 (Ryd)	FAC2 (% diff)
1	$5d^9$	^{2}D	Even	5/2	0.0000	0.0000	0.00	0.0000	0.00
2	$5d^9$	^{2}D	Even	3/2	0.1157	0.1085	− 6.18	0.1096	− 5.28
3	$5d^86s$	^{4}F	Even	9/2	0.2711	0.2484	− 8.38	0.2715	0.13
4	$5d^86s$	^{4}F	Even	7/2	0.3196	0.3000	− 6.15	0.3253	1.77
5	$5d^86s$	^{4}P	Even	5/2	0.3538	0.3485	− 1.50	0.3724	5.27
6	$5d^86s$	^{4}F	Even	3/2	0.3677	0.3599	− 2.12	0.3845	4.57
7	$5d^86s$	^{4}F	Even	5/2	0.4048	0.3874	− 4.31	0.4130	2.02
8	$5d^86s$	^{2}F	Even	7/2	0.4168	0.3981	− 4.49	0.4275	2.55
9	$5d^86s$	^{4}P	Even	1/2	0.4505	0.4610	2.34	0.4845	7.53
10	$5d^86s$	^{4}P	Even	3/2	0.4554	0.4492	− 1.36	0.4751	4.34
11	$5d^86s$	^{2}F	Even	5/2	0.4744	0.4666	− 1.64	0.4952	4.39
12	$5d^86s$	^{2}P	Even	3/2	0.4933	0.4936	0.07	0.5207	5.54
13	$5d^86s$	^{2}G	Even	9/2	0.5269	0.5328	1.12	0.5585	5.99
14	$5d^86s$	^{2}P	Even	1/2	0.5315	0.5423	2.03	0.5715	7.53
15	$5d^86s$	^{2}G	Even	7/2	0.5339	0.5399	1.12	0.5660	6.02
16	$5d^86s$	^{2}D	Even	3/2	0.5802	0.5747	− 0.96	0.6040	4.09
17	$5d^86s$	^{2}D	Even	5/2	0.5854	0.5712	− 2.44	0.6014	2.73
18	$5d^86p$	^{4}D	Odd	7/2	0.8091	0.7585	− 6.25	0.7880	− 2.61
19	$5d^86p$	^{2}G	Odd	9/2	0.8330	0.7942	− 4.66	0.8191	− 1.67
20	$5d^86p$	^{2}D	Odd	3/2	0.8724	0.8455	− 3.08	0.8691	− 0.38
21	$5d^86p$	^{2}F	Odd	5/2	0.8757	0.8403	− 4.04	0.8671	− 0.98
22	$5d^86p$	^{4}D	Odd	5/2	0.9270	0.8779	− 5.29	0.9075	2.10
23	$5d^86p$	^{4}G	Odd	7/2	0.9324	0.8841	− 5.18	0.9129	− 2.09
24	$5d^86p$	^{4}G	Odd	11/2	0.9385	0.8858	− 5.62	0.9155	− 2.46
25	$5d^86p$	^{4}F	Odd	9/2	0.9529	0.9014	− 5.40	0.9327	− 2.12
26	$5d^86p$	^{2}F	Odd	7/2	0.9642	0.9192	− 4.67	0.9486	− 1.62
27	$5d^86p$	^{4}D	Odd	3/2	0.9683	0.9227	− 4.71	0.9534	− 1.54
28	$5d^86p$	^{4}P	Odd	5/2	0.9801	0.9412	− 3.97	0.9697	− 1.06
29	$5d^86p$	^{4}P	Odd	1/2	0.9858	0.9566	− 2.97	0.9818	− 0.41
30	$5d^86p$	^{2}D	Odd	5/2	0.9862	0.9553	− 3.13	0.9810	− 0.52

The relative differences between the energies given by the GRASP^0 and FAC calculations and the literature are shown as a percentage.

As in Au I, we utilized the functionality in GRASP^0 to shift level energies to experimentally determined values. For Au II, the energies of the first 30 energy levels were matched and shifted to their counterparts in Rosberg & Wyart (1997). Table 5 shows a representative comparison of some Au II transition rates with experimental values from Rosberg & Wyart (1997). On average, our GRASP A-values for lines involving the lowest 30 levels agree with those reported in Rosberg & Wyart (1997) within 44 per cent.

2.1.3 Au III

For Au III, only the ground state is available in the NIST ASD, and the most recent work in the area, Zainab & Tauheed (2019), established 262 levels and 1504 transitions with Einstein A-values. 16 configurations were used for our Au III GRASP^0 calculation: the 13 even configurations $5d^9$, $5d^86s$, $5d^86d$, $5d^87s$, $5d^87d$, $5d^76s^2$, $5d^76p^2$, $5d^76d^2$, $5d^77s^2$, $5d^77p^2$, $5d^77d^2$, $5d^76s6d$, and $5d^76s7s$, and the 3 odd configurations $5d^86p$, $5d^87p$, and $5d^76s6p$. In total, this structure encompasses 2783 levels.

A comparison of the lowest 30 levels of Au III from Ehrhardt & Davis (1971) and Zainab & Tauheed (2019) with our GRASP^0 and FAC calculated energies is presented in Table 6. The average difference between the GRASP^0 and the first 30 energies from the literature is 3.6 per cent.

For the calculation of the transition rates, we shifted the first 30 energy levels to energy values from Zainab & Tauheed (2019). Table 5 shows a representative comparison of computed Au III transition rates with experimental values from Zainab & Tauheed (2019); for the 98 transitions common to our GRASP calculations and Zainab & Tauheed (2019), we find that the average difference between the A-values is 42 per cent.

2.2 FAC calculations

To explore the validity and uncertainty quantification of the GRASP^0 calculations, we pursued similar calculations using FAC (Gu 2008). For the GRASP^0 calculations, the choice of configurations was made to most accurately describe the structure while maintaining a reasonably sized basis set for the electron-impact calculations. Employing dozens or hundreds of configurations in a GRASP^0 calculation would increase the computational resources of an electron-impact calculation to unrealistic scales. We have opted to use FAC to investigate the effect of increasing configuration interaction on the fundamental atomic data such as level energies and A-values, and use the FAC results to verify the completeness of the GRASP^0 calculations. The levels and transition rates of Au I–Au III were calculated using the same set of configurations as the respective GRASP^0 calculations, and also explored larger calculations employing dozens of additional configurations.

Within FAC, a single central potential for all configurations is assumed, and atomic state functions are variationally determined as linear combinations of configuration state functions (CSFs). The central potential is typically determined by minimizing the energy of a mean configuration, which is commonly constructed from the ground configuration. However, for the ions considered here, constructing the mean configuration from only the ground state leads to significant errors in both ordering and energies of the excited configurations. We have found that the combination of the ground configuration and two excited configurations for each ion stage improved the agreement between known and calculated energy levels. A similar approach using the ground and two excited configurations to construct the FAC mean configuration was recently reported for W^{8+} (Lu et al. 2021).

We note that small-scale test calculations using the fully frequency-dependent Breit interaction showed little effect on the calculated energies and rates while significantly increasing the computational resources. Therefore, we have utilized a simplified version of the Breit interaction described in the FAC documentation. The electron self-energy was allowed for up to $n = 8$. For each ion stage, all configurations of similar parity were allowed to mix. We have found that the functionality to apply semi-empirical corrections to the energies to correct for errors introduced by the use of a mean configuration (realized in the 'fac.ConfigEnergy' functionality) led to poorer agreement between our GRASP^0 and FAC calculations. Our reported quantities are thus presented without these corrections applied.

As evidenced by significant mixing using the Cowan's code (see e.g. Au II in e.g. Rosberg & Wyart 1997), based upon single configuration determination of orbitals, i.e. Hartree–Fock-Relativistic (HFR) methods, heavy systems such as gold require a treatment of configuration interaction to accurately capture the electronic structure. As the FAC levels are by default output in *jj* coupling, we have used the code *jj2lsj* of Gaigalas et al. (2017), which transforms the *jj*-coupled levels into an approximate *LSJ* coupling scheme. This *jj*-to-*LS* transformation allowed us to match our levels to experimentally derived energies reported in Platt & Sawyer (1941), Ehrhardt & Davis (1971), and Rosberg & Wyart (1997), after which we re-ran the calculations with the matched levels shifted to their experimental values after diagonalization. Thus, *A*-value comparisons to GRASP^0 results are unaffected by the energy scaling inherent in the transition rates (see equation 1), and this allows for a direct comparison of the accuracy of the wavefunctions derived in both calculations.

In the following, the details of our FAC calculations of Au I–Au III levels are provided. For each ion, we first assume the same configurations as those in GRASP^0. We then pursued larger calculations involving >100 configurations for each ion to ensure convergence and determine the accuracy of our GRASP^0 structures that underpin both present and future electron-impact data sets. Lastly, though we have included a significant number of configurations, not all level energies and radiative rates were calculated explicitly. The calculation and printing of energy levels and transition rates was restricted to known configurations or partially known configurations of interest to accommodate the available computing resources. These 'extra' configurations act to modify the wavefunctions and resulting radiative rates through configuration interaction. When transformed from *jj* to *LSJ* coupling, we found that many configurations were strongly mixed as evidenced by low purities in the CSF expansions.

2.2.1 Au I

Our initial FAC configuration set, FAC1 in Table 1, utilized the same configurations as the Au I GRASP^0 calculations. We found the greatest agreement between FAC and GRASP^0 levels when using the mean configuration $5d^{10}6s + 5d^96s^2 + 5d^96s6p$. Using the same mean configuration, we then adopted a larger configuration set, labelled FAC2, which used a total of 63 even and 59 odd configurations involving a select number of single, double, triple, and quadruple excitations with respect to $5d^{10}$ up to $n = 8$. This larger configuration set provided 14 642 CSFs for levels belonging to $5d^{10}6s$ and $5d^96s^2$, and up to 28 369 CSFs for odd parity.

Increasing the configurations from FAC1 to FAC2 leads to an average decrease in the excitation energies of the lowest 26 levels of only 4 per cent while increasing the computation time significantly. An additional calculation (not shown) was carried out involving >200 total configurations, but led to only ∼meV changes in level energies and was thus discarded. After shifting the first 26 levels to their experimentally derived energies, we computed transition rates; comparison of our computed values to the 18 *A*-values available in the NIST ASD yields an average agreement of 52 per cent, with a representative sample reported in Table 3.

2.2.2 Au II

Using only the ground-state configuration $5d^{10}$ to optimize the central potential, we found significant discrepancies in both the energies and ordering between levels identified by Rosberg & Wyart (1997) and our calculations. The agreement between literature and calculated values was significantly improved when using the mean configuration $5d^{10} + 5d^96s + 5d^86s6p$.

Using the above configurations to optimize the potential, our first calculation mirrored the configurations adopted for GRASP^0. For the lowest 30 levels of Au II, we find that the average per cent difference between the FAC and GRASP^0 energies is 5.7 per cent. Using the large FAC2 configuration set (see Table 1) with the change $5d^{10} \rightarrow 5d^9$, the average difference is reduced to 1.7 per cent. This modified 'FAC2' configuration yielded 32 297 CSFs for the even parity, and 49 783 and 64 472 CSFs for the configurations $5d^96p$ and $5d^86s6p$, respectively. The energies for the lowest 30 levels of Au II from the modified FAC2 configuration set are within 5.8 per cent of those reported in Rosberg & Wyart (1997), comparable to the difference between the GRASP^0 energies and Rosberg & Wyart (1997) energies, also 5.8 per cent, for the lowest 30 levels of Au II.

After shifting the lowest 30 levels of Au II to the values in Rosberg & Wyart (1997), we computed transition rates; the geometric mean of $100 \times |A_{\rm FAC} - A_{\rm RW}|/A_{\rm RW}$ for the transitions involving the 30 lowest levels of Au II yields an average agreement of 38 per cent.[1] *gf* values for the 31 allowed $5d^96p \rightarrow 5d^96s$ transitions were also reported in Zhiguo et al. (2002), where lifetimes of $5d^96p$ levels were measured via laser-induced fluorescence and an MCDF calculation including CI provided *gf* values. We find poor agreement between our FAC transition rates and those of Zhiguo et al. (2002), on average 72 per cent. Comparing Zhiguo et al. (2002) and Rosberg & Wyart (1997), these two methodologies also differ by an average of 52 per cent.

Comparison of the GRASP^0 and FAC *A*-values for all E1 transitions between the lowest 30 levels of Au II yields a relative agreement of 11 per cent (linear mean) and 0.68 per cent (geometric mean). Reconciliation of the scatter in Au II transition rates may depend on future computational efforts that include both configuration interaction and core polarization effects, such as the Hartree–Fock

[1]Digitized line list from Rosberg & Wyart (1997) available upon request to sjb0068@auburn.edu

Table 7. Representative comparison of *A*-values from Zainab & Tauheed (2019) compared to the present GRASP^0 and FAC calculations.

Transition levels	Configuration	*A*-value (s^{-1}) GRASP^0	FAC2	Zainab & Tauheed
1 → 18	$5d^9\ ^2D_{5/2} \rightarrow 5d^8 6p\ ^4D^0_{7/2}$	9.56E+04	1.79E+05	8.54E+05
1 → 20	$5d^9\ ^2D_{5/2} \rightarrow 5d^8 6p\ ^2D^0_{3/2}$	4.17E+07	5.16E+07	1.91E+07
1 → 21	$5d^9\ ^2D_{5/2} \rightarrow 5d^8 6p\ ^4D^0_{5/2}$	6.18E+07	3.73E+07	4.13E+07
1 → 22	$5d^9\ ^2D_{5/2} \rightarrow 5d^8 6p\ ^4D^0_{5/2}$	2.09E+07	1.17E+07	9.18E+06
2 → 20	$5d^9\ ^2D_{3/2} \rightarrow 5d^8 6p\ ^2D^0_{3/2}$	4.24E+07	7.27E+06	2.65E+07
2 → 21	$5d^9\ ^2D_{3/2} \rightarrow 5d^8 6p\ ^4D^0_{5/2}$	5.68E+06	3.22E+07	7.35E+06

+ core polarization approach utilized in e.g. Quinet, Palmeri & Biémont (1999).

2.2.3 *Au III*

Zainab & Tauheed (2019) recently studied the arc spectra of Au III and classified 262 levels and 1504 transitions between the even configurations $5d^9$, $5d^8 6s$, and $5d^7 6s^2$ and the odd configurations $5d^8 6p$ and $5d^7 6s6p$. We investigated each possible unique combination of $5d^9$, $5d^8 6s$, $5d^7 6s^2$, $5d^8 6p$, and $5d^7 6s6p$ as a mean configuration for our FAC calculations. The best agreement between the GRASP^0 and FAC calculations was found for the central potential optimized by the mean configuration $5d^9 + 5d^8 6s + 5d^7 6s6p$.

For the initial Au III configuration set, we found a difference between the FAC and GRASP^0 energies for the lowest 30 levels of Au III of 8.3 per cent. Using the larger FAC2 configuration set with the modification $5d^{10} \rightarrow 5d^8$, the average difference between FAC and GRASP^0 improves by a factor of 2, decreasing to 3.8 per cent. We note that the FAC2 calculation for Au III presented computational challenges, requiring breakup into 11 subsets of upper and lower level calculations to fit the available computing resources, after which the energy levels and transition rates were compiled into a single data set. The FAC2 configuration set modified for Au III yielded up to 63 583 CSFs in the even parity and 73 573 CSFs in the odd parity.

Comparing our GRASP and large-scale FAC energies for the 30 lowest levels of Au III to the values reported in Zainab & Tauheed (2019), we find an average difference of 3 per cent (FAC) and 3.6 per cent (GRASP). Before computing transition rates, the lowest 30 levels of Au III were shifted to the experimentally determined values reported in Zainab & Tauheed (2019).

In Zainab & Tauheed (2019), 98 transitions were found to involve the lowest 30 levels of Au III in Table 6. The agreement between the transition rates in FAC and those reported in Zainab & Tauheed (2019) was 36 per cent, calculated as the geometric mean of $100 \times |A_{\rm FAC} - A_{\rm Z\&T}|/A_{\rm Z\&T}$. A representative sample of these *A*-value differences are reported in Table 7. In general, the agreement between our GRASP and FAC *A*-values for E1 transitions between the lowest 30 levels of Au III is 5.25 per cent (linear mean) and 1.15 per cent (geometric mean).

For both Au II and Au III, we find only minor improvements in level energies and transition rates when comparing results of GRASP^0 calculations with a compact configuration set, and FAC calculations involving >100 configurations. The agreement between our small-scale GRASP^0 configuration set and large-scale FAC set validates the use of the GRASP^0 configuration set as the basis for future electron-impact calculations.

3 ELECTRON-IMPACT EXCITATION OF AU I

The underlying theory of electron-impact excitation R-matrix calculations is discussed in greater detail within Burke (2011, relativistic R-matrix theory can be found in section 5.5 'Dirac R-Matrix Theory') and is implemented with the parallel version of the Dirac atomic R-matrix codes as implemented within Ballance (2020) for the Dirac–Coulomb Hamiltonian matrix case.

The electron-impact excitation calculation involved 200 levels out of a possible 2202 levels in the close-coupling expansion of our model for Au I. Low partial waves for neutral gold from $J = 0$–19 of both odd and even parity were calculated in one calculation. Another calculation involving higher partial waves from $J = 20$–35 of both odd and even parity was carried out. It is assumed that the former model represents the possibility of resonance structure and hence would require a finer energy mesh, whilst the higher partial waves would provide a smooth contribution to the total cross-section and would not require such a detailed mesh. Regardless, a top-up procedure (Burgess 1974; Burgess & Tully 1992) is applied to account for higher partial waves $J \geq 35$ to ensure convergence in our total cross-sections and ultimately our Maxwellian-averaged rates. The basis size for each of the continuum angular momentum in both models was 20, and they both spanned the same energy range of the incoming electron. This scattering model involves a maximum of 1242 channels resulting in a number of Hamiltonian matrices with size up to a maximum of 25 759.

One of our goals is to provide a compact smaller data set tailored to the modelling of kilonova studies or NSMs, and therefore we have shifted our first 26 energy levels to their NIST values. This includes the energy levels that we expect to be excited within the temperature and density regime of such astrophysical objects. Of course, both the compact and full models shall be made available within well-known data bases such as OPEN-ADAS (OPEN-ADAS 2021) or CLOUDY (Ferland et al. 2017; Cloudy 2021).

For the lower partial waves from 0.0001 to 1.5 Ryd, there are 15 000 points in the energy grid with a spacing of 0.0001 Ryd; then from 1.5 to 3.0 Ryd, there are 3000 points in the energy grid with a spacing of 0.0005 Ryd. For the higher partial waves from 0.001 to 3.0 Ryd, there are 3000 points in the energy grid with a spacing of 0.001 Ryd while also applying a top-up procedure.

To demonstrate the scope of our electron-excitation calculation, we will utilize the method outlined by Burgess & Tully (1992). This allows one to determine whether it is safe to extrapolate the collision strengths to higher energies and the effective collision strengths to higher electron temperatures. We show some illustrative results for this below. The scaled electron energies are given by

$$x = 1 - \frac{\ln C}{\ln\left(\frac{E_j}{E_{ij}} + C\right)}, \tag{3}$$

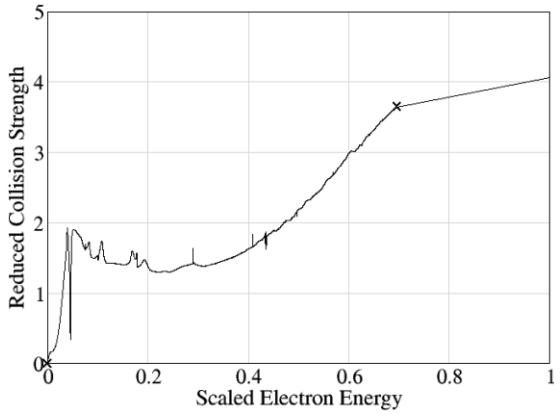

Figure 1. Reduced collision strength for the transition $5d^{10}6s\ ^2S_{1/2} \rightarrow 5d^{10}6p\ ^2P^0_{1/2}$: levels 1 and 4 from Table 2 as a function of scaled electron energy. '×' represents the first and last calculated points.

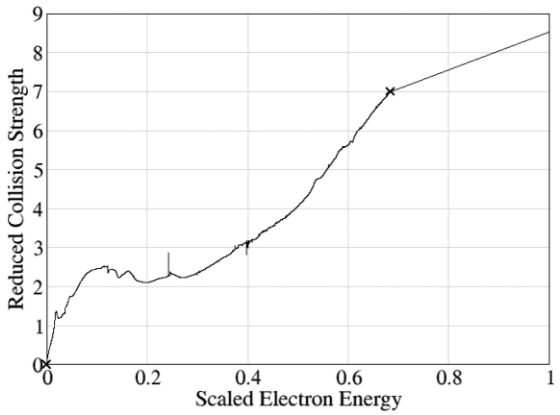

Figure 2. Reduced collision strength for the transition $5d^{10}6s\ ^2S_{1/2} \rightarrow 5d^{10}6p\ ^2P^0_{3/2}$: levels 1 and 5 from Table 2 as a function of scaled electron energy. '×' represents the first and last calculated points.

where E_j is the free electron energy, E_{ij} is the transition energy, and C is an adjustable parameter, which we will set equal to 2. The reduced collision strengths are given by

$$y(x) = \frac{\Omega}{\ln\left(\frac{E_j}{E_{ij}} + e\right)}, \tag{4}$$

where Ω is the collision strength. For the electric dipoles, we also calculated the infinite energy point when the scaled electron energy is equal to 1 as given by

$$y(1) = \frac{4\omega_i f_{ij}}{E_{ij}}, \tag{5}$$

where ω_i is the statistical weight and f_{ij} is the oscillator strength.

Fig. 1 shows the reduced collision strength of the transition between levels $5d^{10}6s\ ^2S_{1/2}$ and $5d^{10}6p\ ^2P^0_{1/2}$, which correspond to levels 1 and 4, respectively, from Table 2. Fig. 2 shows the reduced collision strength of the transition between energy levels $5d^{10}6s\ ^2S_{1/2}$ and $5d^{10}6p\ ^2P^0_{3/2}$, which correspond to levels 1 and 5, respectively, in Table 2. Fig. 3 shows the reduced effective collision strength of the transition between levels $5d^{10}6s\ ^2S_{1/2}$ and $5d^{10}6p\ ^2P^0_{1/2}$, which correspond to levels 1 and 4, respectively, from Table 2. Fig. 4 shows the reduced effective collision strength of the transition between

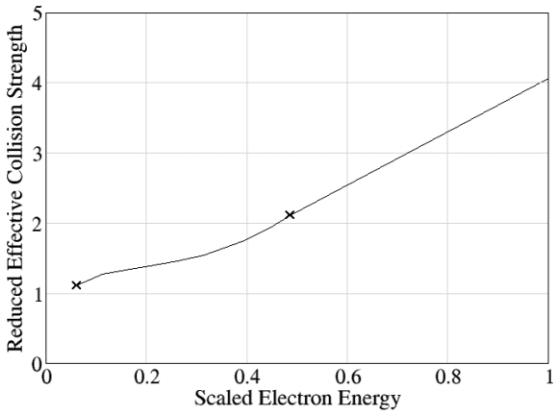

Figure 3. Reduced effective collision strength for the transition $5d^{10}6s\ ^2S_{1/2} \rightarrow 5d^{10}6p\ ^2P^0_{1/2}$: levels 1 and 4 from Table 2 as a function of scaled electron energy. '×' represents the first and last calculated points.

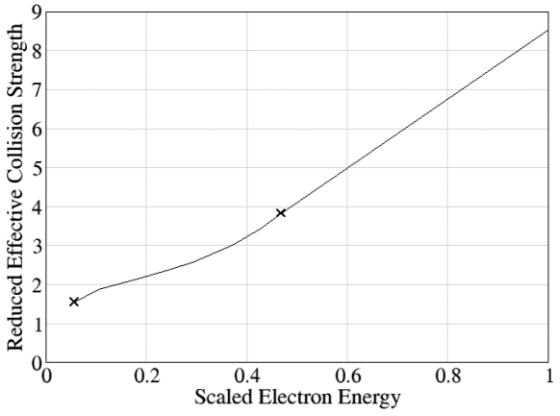

Figure 4. Reduced effective collision strength for the transition $5d^{10}6s\ ^2S_{1/2} \rightarrow 5d^{10}6p\ ^2P^0_{3/2}$: levels 1 and 5 from Table 2 as a function of scaled electron energy. '×' represents the first and last calculated points.

energy levels $5d^{10}6s\ ^2S_{1/2}$ and $5d^{10}6p\ ^2P^0_{3/2}$, which correspond to levels 1 and 5, respectively, from Table 2.

We can see from Figs 1–4 that the collision strengths and effective collision strengths converge towards the infinite energy point at scaled energy equal to 1.

4 COLLISIONAL-RADIATIVE MODELLING OF AU I IN LOW-TEMPERATURE PLASMAS

4.1 Population dynamics

Using the PYTHON collisional-radiative (CR) solver COLRADPY (Johnson, Loch & Ennis 2019), which is based upon CR theory (Bates, Kingston & McWhirter 1962; Summers et al. 2006) and our electron-impact collision rate data, we investigated the excitation dynamics of Au I. We note that this methodology may be extended to any reasonable choice of temperature and density, but we restricted our range of plasma conditions to a range inclusive to those expected at 1–2 d post-merger ($T_e = 1$ eV, $n_e = 10^9$ cm^{-3}, cf. Gillanders et al. 2021). Of principle interest are the population dynamics resulting from electron collisions and their comparison to the assumption of local thermodynamic equilibrium (LTE)-like conditions.

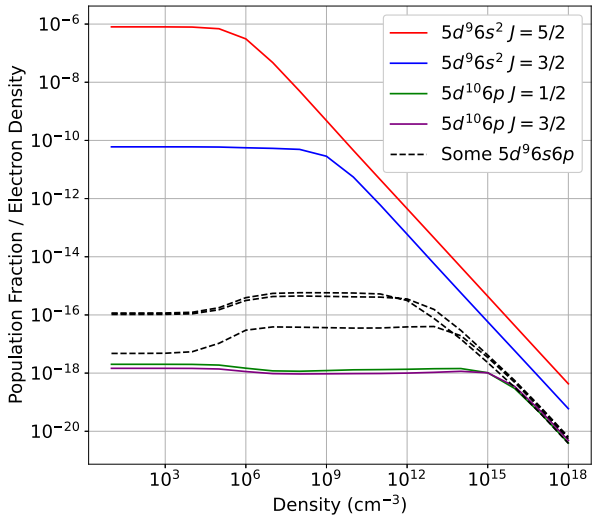

Figure 5. Electron density dependence of excited levels as a function of electron density for a fixed temperature of $T_e = 1$ eV. Here the flat portion represents the coronal regime, and when the gradient is -1, the level is in LTE.

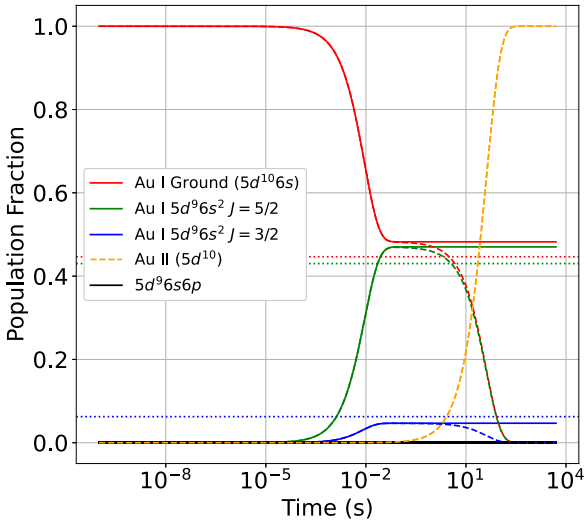

Figure 6. Time dependence of the ground and metastable level population fractions of Au I at $T_e = 1$ eV and $n_e = 4 \times 10^9$ cm^{-3}. Population fractions are shown for no ionization (solid lines) and ionization via ECIP (see text, dashed lines). LTE population fractions at 1 eV are shown as horizontal dotted lines. Excited-state populations (not labelled) are shown as black lines near $y = 0$.

First, Fig. 5 shows the density dependence of some of the excited level populations at a fixed temperature (1 eV). We show here the population fraction divided by electron density to enhance visibility of different excitation regimes. The 'coronal' regime extends up to $n_e \lessapprox 10^5$ cm^{-3}, where populations are linearly dependent on the electron density: Any excitations are immediately followed by radiative decays. Between 10^5 and 10^{11} cm^{-3}, the level populations change non-linearly with electron density and comprise the CR regime. The non-linearity of the populations in this regime means that neither the coronal nor LTE approximations can be made and the full CR matrix must be solved. At higher electron densities, the populations approach their LTE behaviour as reflected by, for example, the linearity of $5d^96s^2$ populations above $\sim 10^{10}$ cm^{-3}. We note that the phrase 'collisional-radiative' is used to describe the regime between the coronal and LTE regimes; however, it should be noted that the CR equations accurately calculate the populations in all three regimes.

For a fixed temperature and density, one can derive an effective equilibrium time-scale from a time-dependent CR calculation. This represents the time required for that population to reach its steady-state value. This is particularly important in determining the time-scale of metastable populations and whether they are likely to have reached steady-state conditions on the time-scale of plasma dynamics. Fig. 6 shows the time evolution of the level populations of Au I at $T_e = 1$ eV and $n_e = 4 \times 10^9$ cm^{-3}. We show the time dependence assuming no ionization (solid lines) and ionization to Au II using exchange classical impact parameter (ECIP) functionality within ColRadPy. As ionization and recombination data are not available for Au I, we focused our remaining efforts on the best-case scenario of no ionization. As shown, by $\sim$50 ms, the ground and metastable populations have reached their steady-state values, which are reasonably close to those expected in LTE (shown as horizontal dotted lines). Excited-state populations (shown in black) are negligible compared to those of $5d^{10}6s$ and $5d^96s^2$.

Lastly, we check the assumption of LTE-valued metastable population fractions across a large range of electron densities at $\sim$eV temperatures. In Fig. 7, the steady-state populations are shown

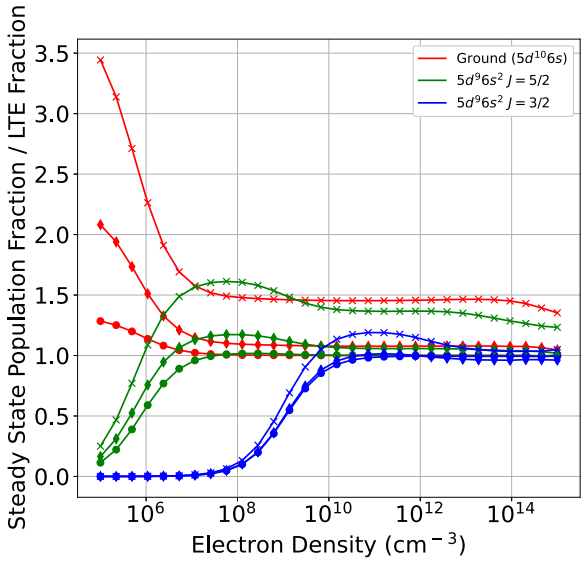

Figure 7. Steady-state population fractions for the ground and metastable levels of Au I divided by their temperature-dependent LTE population fraction at temperatures of 0.5 (°), 1 (◇), and 1.5 eV (×). For each temperature, the populations are normalized so that the total population of the CR and LTE models is each set to 1.

divided by their LTE values as a function of density at temperatures of 0.5 (°), 1.0 (◇), and 1.5 eV (×). For the ground state, the largest deviations occur at low densities regardless of temperature, with the populations slowly approaching the LTE values at higher densities. For the first metastable population with $J = 5/2$, the deviations from LTE are in general $\leq$50 per cent for the conditions expected of observed NSM spectra. However, the second metastable population with $J = 3/2$ shows deviations from LTE as large as a factor of 100 reduction for densities below $\sim 10^{10}$ cm^{-3}.

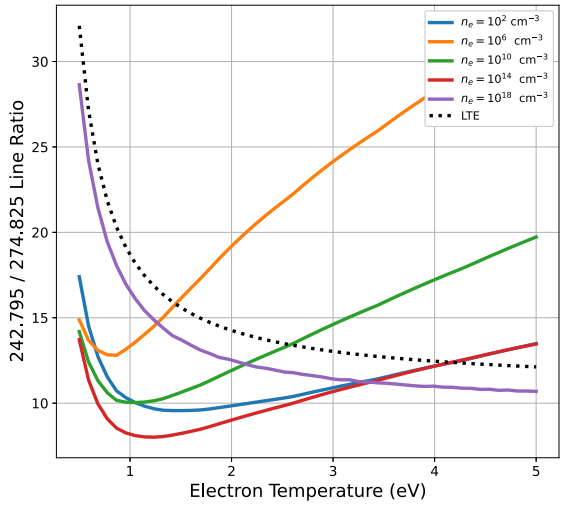

Figure 8. Temperature-dependent line ratio of the resonance line (242.8 nm, $5d^{10}6p \rightarrow 5d^{10}6s$) and the $5d^96s6p \rightarrow 5d^96s^2$ (274.83 nm) line from our CR model (solid lines) and an LTE model (black dashed lines). Transition rates for the lines were shifted to their experimental values (Hannaford, Larkins & Lowe 1981; Fivet et al. 2006). CR line ratios were constructed from the metastable-dependent PECs (Fig. 9) weighted by the metastable population fractions in equilibrium at each set of plasma conditions.

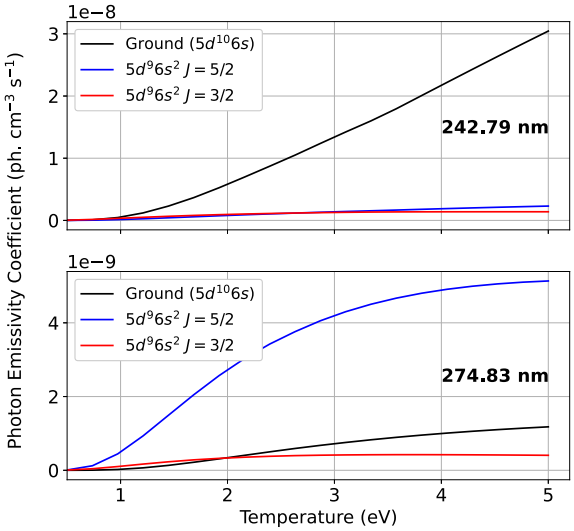

Figure 9. Metastable-resolved PECs for the 242.79 nm resonance line $5d^{10}6p(^2P_{3/2}) \rightarrow 5d^{10}6s(^2S_{1/2})$ (top) and 274.83 nm $5d^96s6p(^4F_{7/2}) \rightarrow 5d^96s^2(^2D_{5/2})$ (bottom). PECs are shown for a fixed density of 1×10^{10} cm^{-3}.

Non-LTE populations, or non-steady-state populations, of the neutral Au metastables that drive the line emission can have a significant effect on the line intensities, indicating that a spectral model that includes accurate metastable fractions must be used. As an example, we show the metastable-resolved photon emissivity coefficients (PECs), calculated in the quasi-static approximation, of the resonance line at 242.79 nm (1 → 5 in Table 3) and the $5d^96s6p \rightarrow 5d^{10}6s$ transition (274.83 nm, levels 2 → 7). We note that the PECs are shown per unit metastable population, i.e. they are not yet weighted by the population fractions of the levels. As shown, the intensity of the resonance line is dominated by excitation out of the ground state, with minimal contribution from excitation of $5d^96s^2$. Alternatively, the 2 → 7 transition is heavily influenced by excitation from the metastable configuration $5d^96s^2$.

Thus, depending on the plasma conditions, if one assumes an LTE model of the line intensities, the populations of both the ground and metastable levels may be in error (cf. Fig. 7), leading to inaccurate line intensities. Fig. 8 shows line ratios of the 242.8 and 274.83 nm lines, constructed from the PECs in Fig. 9, as a function of temperature. The *A*-values for these two lines were shifted to their literature values (Hannaford et al. 1981; Fivet et al. 2006) for completeness. Depending on the plasma conditions, the line ratio deviates from its LTE value by as much as a factor of 3. The non-linearity of the line ratio with increasing density (at constant temperature) is driven by the sensitivity of the $5d^96s^2$ metastable level to electron density. This line ratio is shown only as a representative example of the influence of non-LTE metastable populations, and a more accurate prediction of the line ratio in astrophysical plasmas may require consideration of other collisional processes (such as recombination) that may affect the collision dynamics.

We investigated effects of an expanded electron-impact data set (200 levels) and found negligible differences in level populations at low electron temperatures (∼eV) across a wide range of densities. Several lines above 400 nm show ∼25 per cent increases in line intensity resulting from cascade effects, but these lines are weak and the effect on the possibly observed lines (discussed below) is negligible.

4.2 Diagnostic line ratios

Metastable-resolved PECs offer many diagnostic possibilities. If two lines are dominated by the same excitation channel, e.g. driven directly from ground, their ratio is independent of the metastable populations and is a direct indicator of the local temperature and/or density. Alternatively, line ratios with differing excitation mechanisms, for example, one driven from ground and one driven from a metastable level such as in Fig. 9, can be used to derive metastable population fractions and examine the deviations from LTE conditions. Therefore, we investigated the diagnostic capabilities in terms of line ratios generated by our electron-impact data set in the low-temperature and low-density regime. For each important configuration, we discuss possible diagnostic lines in turn.

The excited configuration $5d^{10}6p$ has two possible decays to the ground level (242.79 and 267.59 nm) and four possible decays to metastable $5d^96s^2$. The resonance line is dominated by excitation from the ground level with a weak dependence on density and a moderate dependence on temperature. Combined with its strength, this line is an excellent candidate for ultraviolet (UV)-based temperature diagnostics. The second 6p level ($J = 1/2$) is weakly dependent on metastable populations and shares similar temperature/density characteristics. Two decays from $5d^{10}6p$ to metastable $5d^96s^2$ have comparable PECs to other strong transitions, but only one (312 nm) is near other identified diagnostic lines. This transition is primarily driven (> 70 per cent) by the ground population and could form the basis of a line ratio diagnostic.

The configuration $5d^96s6p$ contains the most significant diagnostic potential. The 63 possible decays from $5d^96s6p$ to the ground and metastable levels span 151–482 nm with over two dozen having PECs within a factor of 100 of that of the strongest line (resonance, 242.79 nm). Contrasting with the ground-dominant PEC behaviour of $5d^{10}6p$, many of the lines from $5d^96s6p$ exhibit strong dependences on the population of one or both metastable levels.

We have identified the strongest lines from the configuration $5d^96s6p$, i.e. their weighted and summed PEC is ≥1/100 that of the

Table 8. Potential diagnostic lines of Au I at NSM conditions.

Vacuum wavelength (nm)	Upper level index	Lower level index	Populating channel	Sensitivity
178.235	20	1	1	T_e
179.429	19	1	0 + 1	T_e
187.983	17	1	0 + 1	T_e
191.961	26	2	2∗	n_e
195.192	13	1	1	T_e
201.271	22	2	2	n_e, T_e
202.202	21	2	1	T_e
212.732	10	1	1	T_e
213.017	20	2	1	T_e
229.142	16	2	1	T_e
235.334	15	2	2	n_e, T_e
236.274	14	2	2	n_e, T_e
237.697	13	2	1	T_e
238.848	12	2	1∗	T_e
242.868	5	1	1	T_e
261.246	23	3	1 + 2	T_e
264.227	10	2	1	T_e
267.673	4	1	1	T_e
268.688	9	2	1∗	T_e
270.170	8	2	1∗	T_e
274.907	7	2	1∗	T_e
303.009	6	2	1∗	T_e
312.369	5	2	1	T_e
332.781	14	3	2∗	n_e, T_e
335.612	13	3	1	T_e
400.900	9	3	1∗	T_e
404.207	8	3	1∗	T_e

Level indexing follows that provided in Table 2. The dominant populating channels are listed as ground (0), first metastable (1), and second metastable (2). Lines that are overwhelmingly driven by excitation from a single lower level population are denoted by '∗'.

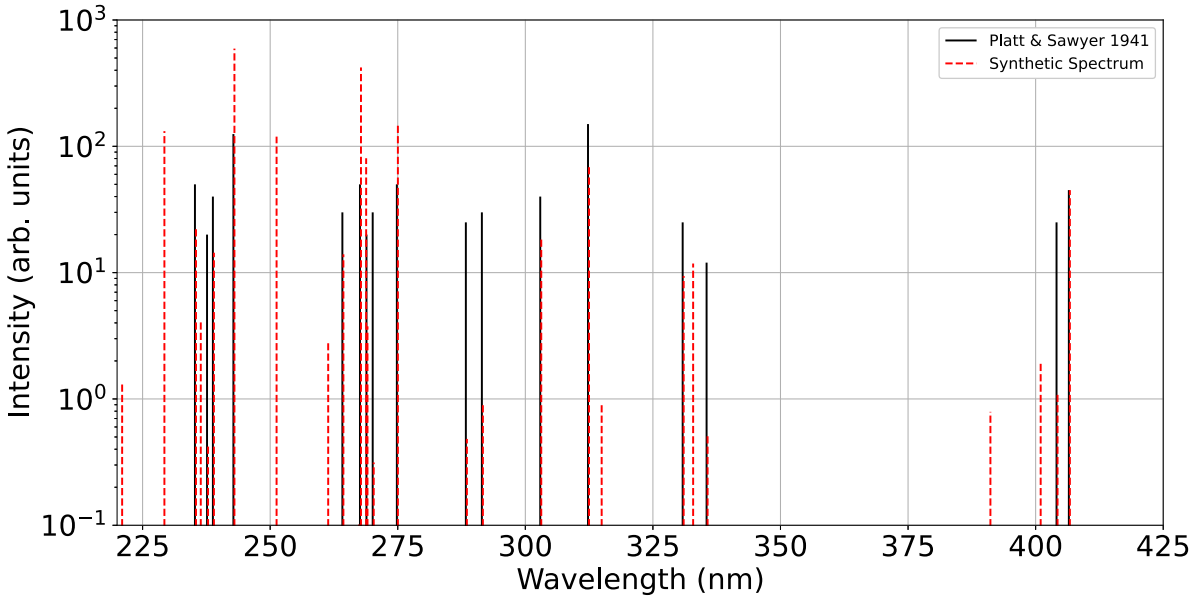

Figure 10. Synthetic spectra of Au I (dashed red lines) generated at $T_e = 3.1$ eV and $n_e = 2.7 \times 10^{13}$ cm^{-3} compared to observed line intensities in Platt & Sawyer (1941, solid black lines) on a logarithmic scale. The synthetic spectra are shifted + 0.2 nm for visibility and arbitrarily scaled to the $5d^{10}6d \rightarrow 5d^{10}6p$ line at 406.5 nm, which is unlikely to be optically thick (see text).

strongest line (resonance). In Table 8, we list these lines alongside those of $5d^{10}6p$, which span 178–404 nm. For each line, the indexing scheme follows that adopted for Table 2, where we have also indicated the dominant populating channel and particular sensitivities to either/both electron density and temperature. In this temperature regime, each line is sensitive to temperature as excitation channels begin to open for T_e of the order of 0.5–1 eV.

Surprisingly, only two of the $5d^96s6p$ lines are dominated by excitation from the ground level, with another two strongly influenced by the ground and first metastable levels. Eight lines, spanning the range 237–404 nm, are dominated by excitation from the first metastable, with only three total lines in our data set uniquely sensitive to the second metastable population at NSM-like conditions. Potential density-sensitive lines exclusively consist of those driven by excitation from the second metastable level of Au I. This is caused by the strong density dependence of the $J = 3/2$ metastable population (cf. Fig. 7). The proximity of many of these lines to the three strong $5d^{10}6p$ decays in the UV and the ground-dominated PECs of $5d^{10}6p$ lines leads to $5d^{10}6p/5d^{10}6s6p$ line intensity ratios forming strong temperature, density, and metastable population diagnostics.

Lastly, the excited even configuration, $5d^{10}6d$, can E1 decay to odd configurations $5d^{10}6p$ and $5d^96s6p$. For the three allowed $5d^{10}6d \rightarrow 5d^{10}6p$ decays, the PECs are dominated by the ground state and may form the basis of future temperature diagnostics in laboratory plasmas. The $5d^{10}6d \rightarrow 5d^96s6p$ lines are weak at the low electron temperatures considered here.

5 EXPERIMENTAL BENCHMARKING

Comparisons of the FAC and GRASP^0 calculations show typical differences of the order of10 per cent or less for energies and transition rates. We tested our electron-impact data set by comparing synthetic spectra against known line intensities of a low-temperature (few eV) gold plasma. Platt & Sawyer (1941) reported a comprehensive line list of neutral gold, which was observed in a hollow cathode discharge at 300 mA lamp current in an ∼10 Torr atmosphere of He gas. They also reported line information for the levels in Table 2 in addition to higher excited configurations, including Rydberg series of the form $5d^{10}nl$ and the auto-ionizing configuration $5d^96s6d$. While the electron densities are likely orders of magnitude higher than those expected in NSM plasmas, the low temperature allows for testing of our diagnostic lines at approximately eV temperatures.

In Platt & Sawyer (1941), the authors used four different spectrographs and do not note any procedure for extracting intensities from their photographic plates, and the data are likely uncorrected for intensity response. Two problems are readily apparent: Disagreements in the line ratio for the 242.8 and 312.3 nm decays of $5d^{10}6p\ ^2P_{3/2}$ suggest optically thick conditions for the line ratio. If the conditions were optically thin, the line ratio would be 10 (in accordance with measured A-values) or 20 (using our calculated A-values), but is 0.8 according to the reported intensities in Platt & Sawyer (1941). In addition, the $5d^{10}7s \rightarrow 5d^{10}6p$ transition at 751 nm is a factor of 20 stronger than expected, suggesting significant changes in intensity response from the UV to the near-infrared region. Test calculations using the escape factor method ('ADAS214'), where we assume (to first order) $n_{Au} \sim n_e \sim 10^{14}$ cm^{-3}, suggest significant absorption of the resonance line, reducing the expected A-value ratio from 10 to ∼2. We have thus focused our efforts on diagnosing their plasma conditions using only close-lying lines most likely to be unaffected by opacity effects in order to minimize wavelength- and opacity-dependent complications.

First, we investigated each unique line ratio constructed from lines common to our data set and Platt & Sawyer (1941). Contour plots of agreement between synthetic and measured line ratios in density–temperature space were generated. The possible line ratios suggest reasonable plasma conditions, with the electron temperature T_e spanning ∼1–4 eV and electron densities in the range 10^{11}–10^{15} cm^{-3}. We attribute this large initial range to uncertainties in the model data (transition rates and electron-impact data) and the unknown intensity scale of Platt & Sawyer (1941). The strength of the absorption effects inferred from lines involving the ground level suggests electron densities at the median of the range above.

While the relative heights of individual lines may be in error due to uncertainty in our transition rates, the inaccuracies are suppressed when considering many line ratios simultaneously. We narrowed the candidate diagnostic lines in this data set to those that are close in wavelength, differing by no more than 30 nm, that do not involve the ground level. With these conditions enforced, the number of lines usable for diagnosing the plasma conditions is reduced to several dozen. A further reduction of the parameter space is achieved by enforcing a requirement of greater than 20 intensity (on the scale reported by Platt & Sawyer 1941).

Five lines were ultimately chosen to diagnose the plasma conditions – 238.775, 264.148, 302.92, 312.278, and 330.83 nm – the latter four of which benefit from the fact that only one spectrograph described by Platt & Sawyer (1941) is capable of measuring these lines, suggesting that they share a common intensity response. From these line ratios, we derived the plasma conditions $T_e = 3.1 \pm 1.2$ eV and $n_e = 2.7^{+1.3}_{-0.9} \times 10^{13}$ cm^{-3}.

Fig. 10 shows a comparison of the synthetic spectra (scaled to the 406.5 nm $5d^{10}6d$ decay to $5d^{10}6p$) versus the intensities reported by Platt & Sawyer (1941) at these plasma conditions. The scaling to a $5d^{10}6d \rightarrow 5d^{10}6p$ line is chosen as the line is unaffected by opacity effects at these conditions. Good absolute agreement is unexpected across the full wavelength range, but relative agreement in line heights is achieved for strong lines nearby in wavelength space.

While the plasma conditions of Platt & Sawyer (1941) are at several orders of magnitude higher electron density than expected in NSM environments, our comparison shows the applicability of our simplified data set to a wide range of plasma conditions up to several eV electron temperature. Using our compact data set, a comparison to the spectra of Bromley et al. (2020) is difficult due to higher temperatures of the order of ∼30 eV (cf. Johnson, Loch & Ennis 2020). At these temperatures, cascades from higher excited states have a significant effect on the spectra, and an expanded electron-impact data set must be utilized. Additionally, the recording of the spectra reported in Bromley et al. (2020) was conducted to identify emission from highly excited states, but each wavelength range (40 nm) was recorded for separate discharges with variable plasma conditions, and the fast time-scale of data collection led to problematic saturation of key diagnostic lines such as the resonance 242 nm transition. Future experiments are planned using the same apparatus and a solid gold target with the intent of identifying additional lines of Au I and Au II while optimizing the wavelength ranges to enable diagnosis of the plasma conditions within each discharge. Future electron-impact data sets for Au II and Au III will aid this effort and expand the use of our data to higher temperature environments.

6 CONCLUSIONS

We calculated the electronic structures of Au I–Au III using the GRASP^0 and FAC codes. Differences between the two codes were generally < 10 per cent, where the large-scale FAC calculations validate

the smaller configuration set adopted for the GRASP^0 calculations. Using the smaller GRASP^0 configuration set, electron-impact collision strengths were calculated for the important configurations of Au I expected to be excited at NSM-like plasma conditions. The electron-impact excitation calculation consisted of a 200 level model, which was then reduced further to a 26 level model, including the important configurations for the purpose of CR modelling. *adf04* files from each model will be made available on the OPEN-ADAS data base (OPEN-ADAS 2021).

Using our electron-impact data set for Au I, we investigated the collisional dynamics of neutral gold at conditions expected in NSM ejecta, T_e < few eV and $n_e \leq 10^{11}$ cm^{-3}. We report an upper bound on the collisional equilibrium time-scales for the ground and metastable populations of the order of ∼50 ms, suggesting that any synthesized gold is in collisional equilibrium. At densities $\lessapprox 10^{10}$ cm^{-3}, significant deviations as high as a factor of 100 are found for the metastable populations of $5d^9 6s^2$. For many of the strongest lines of Au I, excitation from metastable $5d^9 6s^2$ is comparable to or exceeds the contribution of direct excitation from the ground level, suggesting that any LTE-derived line ratios may be in error. We identified 27 strong lines of Au I in the UV–Vis range, which may form the basis of temperature, density, and metastable population diagnostics.

We presented an experimental test of our electron-impact data set by diagnosing the plasma conditions of the Au I spectra reported in Platt & Sawyer (1941). Disagreements between the modelled and observed line intensities for the resonance lines suggest optically thick conditions for lines involving the ground level. Using the observed line intensities of close-lying lines excited from metastable levels unlikely to be affected by optically thick conditions, we diagnosed the plasma conditions as $T_e = 3.1 \pm 1.2$ eV and $n_e = 2.7^{+1.3}_{-0.9} \times 10^{13}$ cm^{-3}, consistent with the conditions required to produce optically thick conditions for resonance lines.

Future work will expand the calculation of electron-impact excitation data to singly and doubly ionized gold based upon the GRASP^0 structure calculations described in Sections 2.1.2 and 2.1.3. These data sets will be tested at both existing and future measurements of high-temperature gold discharges comparable to Bromley et al. (2020). Using electron-impact data, we hope to find useful diagnostic lines for singly and doubly ionized gold as we have done for neutral gold. Similarly, we will investigate the inclusion of higher excited states to determine the effect of cascades on low-lying diagnostic lines at high electron temperatures.

ACKNOWLEDGEMENTS

This work was funded by the Science and Technology Facility Council (STFC) through the Queen's University Belfast Astronomy Observation and Theory Consolidated Grant 2020-2023 ST/T000198/1. The authors (SDL and SB) gratefully acknowledge funding support from the National Science Foundation grant number 1816984. Calculations were carried out on the Hawk supercomputer at the High-Performance Computing Center Stuttgart (HLRS) as well as on a local cluster at the Queen's University Belfast. The authors also gratefully acknowledge the support and computing resources provided by the Auburn University Hopper Cluster.

DATA AVAILABILITY

The data presented in this work will be made available in the OPEN-ADAS data base in the form of adf04 files compatible with the ADAS suite of codes or the open-source COLRADPY (Johnson et al. 2019).

REFERENCES

Ballance C. P., 2020, R-matrix codes. http://connorb.freeshell.org
Bates D. R., Kingston A. E., McWhirter R. W. P., 1962, Proc. R. Soc. A, 267, 297
Bromley S. J. et al., 2020, ApJS, 250, 19
Burgess A., 1974, J. Phys.B: At. Mol. Opt. Phys., 7, L364
Burgess A., Tully J. A., 1992, A&A, 254, 436
Burke P. G., 2011, Springer Series on Atomic, Optical, and Plasma Physics. Vol. 61, R-Matrix Theory of Atomic Collisions: Application to Atomic, Molecular and Optical Processes. Springer-Verlag, Berlin
Cloudy, 2021, Cloudy, https://gitlab.nublado.org/cloudy/cloudy/-/wikis/home
Coulter D. A. et al., 2017, Science, 358, 1556
Cowan R. D., 1981, The Theory of Atomic Structure and Spectra. Univ. California Press, Berkeley, CA
Ehrhardt J. C., Davis S. P., 1971, J. Opt. Soc. Am., 61, 1342
Ferland G. J. et al., 2017, Rev. Mex. Astron. Astrofis., 53, 385
Fivet V., Quinet P., Biémont É., Xu H. L., 2006, J. Phys. B: At. Mol. Opt. Phys., 39, 3587
Fontes C. J., Fryer C. L., Hungerford A. L., Wollaeger R. T., Korobkin O., 2020, MNRAS, 493, 4143
Gaigalas G., Froese Fischer C., Rynkun P., Jönsson P., 2017, Atoms, 5, 6
Gillanders J. H., McCann M., Sim S. A., Smartt S. J., Ballance C. P., 2021, MNRAS. 506, 3560
Gu M. F., 2008, Can. J. Phys., 86, 675
Hannaford P., Larkins P. L., Lowe R. M., 1981, J. Phys. B: At. Mol. Phys., 14, 2321
Hartwell G., Knowlton S., Hanson J., Ennis D., Maurer D., 2017, Fusion Sci. Technol., 72, 76
Johnson C., Loch S., Ennis D., 2019, Nucl. Mater. Energy, 20, 100579
Johnson C. A., Loch S. D., Ennis D. A., 2020, Plasma Phys. Control. Fusion, 62, 125017
Kajino T., Aoki W., Balantekin A., Diehl R., Famiano M., Mathews G., 2019, Prog. Part. Nucl. Phys., 107, 109
Kramida A., 2019, Atoms, 7, 64
Kramida A., Ralchenko Y., Reader J., NIST ASD Team, 2020, NIST Atomic Spectra Database (version 5.8). https://physics.nist.gov/asd
Lu Q. et al., 2021, Phys. Rev. A, 103, 022808
OPEN-ADAS, 2021, OPEN-ADAS, https://open.adas.ac.uk
Parpia F. A., Froese Fischer C., Grant I. P., 1996, Comput. Phys. Commun., 94, 249
Platt J. R., Sawyer R. A., 1941, Phys. Rev., 60, 866
Quinet P., Palmeri P., Biémont E., 1999, J. Quant. Spectrosc. Radiat. Transfer, 62, 625
Rosberg M., Wyart J.-F., 1997, Phys. Scr., 55, 690
Summers H. P. et al., 2006, Plasma Phys. Control. Fusion, 48, 263
Uylings P., Raassen T., 2019, Atoms, 7, 102
Zainab A., Tauheed A., 2019, J. Quant. Spectrosc. Radiat. Transfer, 237, 106614
Zhiguo Z., Brage T., Curtis L. J., Lundberg H., Martinson I., 2002, J. Phys. B: At. Mol. Opt. Phys., 35, 483

SUPPORTING INFORMATION

Supplementary data are available at *MNRAS* online.

adf04_AuI

Please note: Oxford University Press is not responsible for the content or functionality of any supporting materials supplied by the authors. Any queries (other than missing material) should be directed to the corresponding author for the paper.

This paper has been typeset from a TEX/LATEX file prepared by the author.